Chaos

Simplified description of dynamics in neuromorphic resonant tunneling diodes

I. Ortega-Piwonka, A. E. Teruel, R. Prohens, et al.

View Online   Export Citation   CrossMark

ARTICLES YOU MAY BE INTERESTED IN

Simplified description of dynamics in neuromorphic resonant tunneling diodes

View Online   Export Citation   CrossMark

I. Ortega-Piwonka,[1,2,a] A. E. Teruel,[1,3] R. Prohens,[1,3] C. Vich,[1,3] and J. Javaloyes[1,2]

AFFILIATIONS

[1] Institute of Applied Computing and Community Code (IAC-3), University of the Balearic Islands, Carretera de Valldemossa, km. 7.5, Palma 07122, Spain
[2] Department of Physics, University of the Balearic Islands, Carretera de Valldemossa, km. 7.5, Palma 07122, Spain
[3] Department of Mathematics and Computer Science, University of the Balearic Islands, Carretera de Valldemossa, km. 7.5, Palma 07122, Spain

[a] Author to whom correspondence should be addressed: ignacio.ortega.piwonka@gmail.com

ABSTRACT

In this article, the standard theoretical model accounting for a double barrier quantum well resonant tunneling diode (RTD) connected to a direct current source of voltage is simplified by representing its current–voltage characteristic with an analytically approachable, anti-symmetric N-shaped function. The time and variables involved are also transformed to reduce the number of parameters in the model. Responses observed in previous, more physically accurate studies are reproduced, including slow–fast dynamics, excitability, and bistability, relevant for spiking signal processing. A simple expression for the refractory time of the excitable response is derived and shown to be in good agreement with numerical simulations. In particular, the refractory time is found to be directly proportional to the circuit's intrinsic inductance. The presence or absence of bistability in the dependence of the parameters is also discussed thoroughly. The results of this work can serve as a guideline in prospective endeavors to design and fabricate RTD-based neuromorphic circuits for power and time-efficient execution of neural network algorithms.

Published under an exclusive license by AIP Publishing. https://doi.org/10.1063/5.0062686

Nanoscale resonant tunneling diodes have a potential application as fundamental units (i.e., nodes) in spiking neuromorphic processors given their locally negative differential conductance, small size, and high frequency. In prior theoretical studies,[1–3] a resonant tunneling diode connected to DC voltage has been demonstrated as a class-2 excitable spike generator (i.e., excitability is achieved when the circuit is biased in proximity to an Andronov–Hopf bifurcation[4]). In these works, the non-ohmic current–voltage characteristic is represented by Schulman's formula[5] that, while physically accurate, is also analytically complex. Here, a more simple, anti-symmetric, N-shaped current–voltage characteristic, made by a linear function minus a sigmoid, is used instead. This, together with the normalization of the time and variables involved in the equations, provides a simplified model with a reduced number of parameters that reproduces most of the typical responses reported in the works mentioned above. The simplified model also allows for an approachable description of the equilibrium solutions and their transitions in terms of the parameters on the analytical, numerical, and geometrical basis. In particular, the model may or may not exhibit a coexistence of fixed-value response with self-oscillations (i.e., bistability), which represents a hindrance for the purpose of excitable spike generation. Based on an adiabatic approximation and slow–fast dynamics, an analytically simple expression for the refractory time (i.e., the duration of the excitable spike) is integrated. This expression is shown to be directly proportional to the circuit's intrinsic inductance and is in good agreement with numerical simulations.

I. INTRODUCTION

During the last years, the field of Artificial Intelligence (AI) has experienced an explosive growth. Every day, neural networks and machine learning algorithms find new applications in both industry and academic research studies, with the subsequent increase in the

demand for competent professionals and hardware. Nonetheless, one of the most significant obstacles that stagnates these applications lies on the very architecture modern computers are designed under, inspired by the Von Neumann model and the Complementary Metal Oxide Semiconductor (CMOS) technology. The cornerstone behind AI is learning by mining and analyzing large amounts of pre-existing data, and current computers are able to execute these algorithms only at the cost of long waiting times and high energy consumption. The causes are numerous and include the inability of processors to distinguish instructions from data, unnecessary data displacements between physically distant units within integrated circuits, and heat dissipation in electronic junctions.

Several efforts are being carried out with the purpose of designing a new architecture able to meet the requirements discussed above. Examples include the IBM TrueNorth chip[6] and Intel Quark SE chip[7] as well as an optoelectronic implementation by Robertson et al.[8] and an all-optical implementation by Feldmann et al.[9] These projects share a common core idea: to emulate the dynamics of the Human brain and neurons, based upon generation and propagation of short voltage spikes at arbitrary moments. This is possible because neurons are *excitable systems*, i.e., they respond to an external stimulus solely in the case that such stimulus is stronger than a certain threshold. The response is complex and drives the system far away from its natural state of equilibrium, but only for a short span (in the ms range), known as *refractory time*.[4,10,11] During the refractory time, the system is unable to respond to any subsequent stimulus, regardless of its strength. Data processing in the form of excitable spikes has the expressiveness of analogical signaling and the advantage of lower energy consumption and robustness in the presence of noise, proper of digital signaling.

A fast, low-power spike-signaling architecture based on resonant tunneling diodes (RTDs) has been proposed in previous works.[1,12] An RTD is a non-ohmic device with a highly nonlinear current–voltage characteristic, resulting from its multi-layer semiconductor structure, aimed to produce a double barrier quantum well (DBQW). An incident electron may cross the DBQW with a probability that is locally maximized if its Fermi energy level matches one of the confinement eigen-energy levels of the barrier. Consequently, the current intensity across the RTD exhibits local maximal points at finite, nonzero voltages, with local minimal points in between. This in turn defines regions of positive differential conductance (PDC) and negative differential conductance (NDC). This property allows RTDs to exhibit self-oscillations in response to a direct current (DC) input. Indeed, RTDs are the smallest and fastest oscillators up to date, able to emit signals in the terahertz (THz) frequency range.[13,14] The potential of RTDs in ultrahigh-rate digital signaling has been vastly explored.[15,16] However, an RTD can also behave as an excitable spike generator with the proper specifications and configuration.[1–3,17] With this in mind, nanoscale RTDs can be used as single units (i.e., nodes that emulate the dynamics of a spiking neuron) in RTD-based neuromorphic processors, which could in turn execute machine learning and neural network algorithms efficiently.

On this regard, it is essential to have an understanding of the responses that RTD-based circuits exhibit in terms of the parameters that define them. To this end, a theoretical model is proposed

by Romeira et al.[1] that describes the dynamics of an RTD connected to electrical and optical inputs. The model includes an analytical expression accounting for the current–voltage characteristic provided by Schulman.[5] This formula is derived by applying the Fermi–Dirac statistics in an idealized DBQW-RTD with a single NDC region embedded in between two PDC regions, separated by one peak and one valley. Thus, the I–V characteristic has a well-known N-shaped profile like those typically observed in micro- and nanoscopic RTDs.[13–16] Romeira's model with Schulman's curve is also studied in a successive work,[2] where a wide variety of phenomena, such as self-oscillations, slow–fast dynamics, bistability, mixed-mode oscillations (MMOs), and localized structures, are discussed. In a following work by Ortega et al.,[3] the model is used to emulate an RTD connected to a DC voltage source, and the responses in terms of the system's parameters are thoroughly described.

The studies discussed above have proven to be difficult from the analytical point of view, given the complexity of Schulman's curve. Therefore, it would be desirable to have a more simple expression to represent the I–V characteristic that retains its N-shaped profile and reproduces the observed phenomena that are key to spike signaling: excitability, slow–fast self-oscillations, and bistability. (The presence of bistability is detrimental for the purpose of spike generation because it may lead to bursting.[4]) The FitzHugh–Nagumo model, which makes use of an N-shaped, third-degree polynomial as the current–voltage characteristic,[18,19] seems to be the most befitting choice. However, this model does not exhibit bistability when the circuit's resistance is low. In addition, the N-shaped third-degree polynomial is unique (save normalization) and its shape cannot be tuned. This is relevant to bistability because its presence or absence depends sensitively on the second and third derivatives of the I–V characteristic.[20] To capture these elements, we propose a simplified model with a tunable, N-shaped I–V characteristic consisting of a linear function minus a sigmoid. Such a curve lacks the physical foundations of Schulman's formula, and it is not suitable for quantitatively reproducing (or fitting) the I–V characteristic of micro- and nanoscale RTDs. However, it allows for our model to provide a qualitatively reliable and comprehensible description of the RTD's responses in terms of a reduced number of parameters and reproduces the phenomena that are key to spike signaling. Finally, a simple analytical expression for the refractory time of the excitable response is computed in terms of the model parameters. A short refractory time is desirable in order to transmit a large amount of information in the form of excitable spikes in a short time span.

The article is structured as follows. In Sec. II, the theoretical model and current–voltage characteristic used are described in detail, as well as the parameters and equilibrium solutions. This simplified model reproduces slow–fast dynamics and excitability, as explained in Sec. III. A thorough discussion on the model responses in terms of its parameters is provided in Sec. IV. Bistability is discussed in Sec. V. An analytical expression for the self-oscillation period in the slow–fast regime is derived in Sec. VI, which leads to a more simple expression for the refractory time. A summary and final discussions are presented in Sec. VII.

II. SIMPLIFIED RTD MODEL

A. Derivation of the simplified model

We start with the standard physical model accounting for the dynamics of a double barrier quantum well resonant tunneling diode (DBQW-RTD or RTD for short) connected to a DC source of voltage,

$$C\frac{dV}{dt} = I - F(V), \tag{1}$$

$$L\frac{dI}{dt} = V_0 - V - RI. \tag{2}$$

Equations (1) and (2) are derived from the laws of Kirchhoff. Figure 1 shows a scheme of the circuit. Here, $V(t)$ and $I(t)$ are the voltage and current across the RTD. V_0 is the input bias DC voltage. R, L, and C are the circuit's intrinsic resistance, inductance, and capacitance. $F(V)$ is the RTD nonlinear, N-shaped current–voltage characteristic. This curve tends to be irregular and rough in micro- and nanoscale RTDs and more so in the latter, where the quantum effects are more pertinent (see Fig. 1). However, they typically exhibit a region of negative differential conductance (NDC) embedded in between two regions of positive differential conductance (PDC). In prior studies,[1–3] $F(V)$ has been represented by using an analytical expression derived by Schulman.[5] The solutions in equilibrium are characterized and responses that suggest potential applications in spiking signal processing (namely, slow–fast dynamics, excitability, and bistability) are identified. Schulman's formula is physically accurate and suitable for experimental fitting, but it is analytically complex and has a large number of parameters (which add to R, L, C, and V_0). Instead, we introduce a simple N-shaped expression that allows for a minimal model with a reduced number of parameters, able to qualitatively reproduce the same phenomena and provide analytically simple descriptions. The following properties are assumed on $F(V)$, which will be necessary in the steps leading to the simplified model:

- $F(V)$ has a single NDC region embedded in between two PDC regions, delimited by peak and valley voltages V_p and V_v, with $0 < V_p < V_v$. This confers an N-shaped profile to $F(V)$.
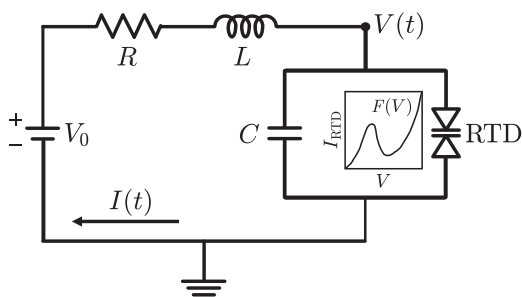

FIG. 1. Schematics of a DBQW-RTD connected to a DC source of voltage, together with a typical current–voltage characteristic observed in micro- and nanoscale devices.

- $F(V)$ is anti-symmetric with respect to the NDC region central axis; i.e., given $V_c = \frac{1}{2}(V_p + V_v)$, it follows that $F(V_c - V) = -F(V_c + V)$ for all V.
- The (negative) differential conductance $F'(V)$ is minimal at $V = V_c$.

After defining a normalized time $\tau = t/\sqrt{LC}$ and a coefficient $\mu = \sqrt{C/L}$, Eqs. (1) and (2) read

$$\mu\frac{dV}{d\tau} = I - F(V), \tag{3}$$

$$\frac{dI}{d\tau} = \mu(V_0 - V - RI). \tag{4}$$

It is explained in the study of Ortega *et al.*[3] that μ levels the stiffness of the dynamics in the circuit. Note that the system of Eqs. (3) and (4) has three parameters instead of four. This system is also invariant under translations along both voltage and current axes. Indeed, after defining, $\mathcal{V} = V - V_c$, $\mathcal{I} = I - F(V_c)$, $\mathcal{V}_0 = V_0 - V_c - RF(V_c)$, and $\mathcal{F}(\mathcal{V}) = F(V) - F(V_c)$, Eqs. (3) and (4) read as

$$\mu\frac{d\mathcal{V}}{d\tau} = \mathcal{I} - \mathcal{F}(\mathcal{V}), \tag{5}$$

$$\frac{d\mathcal{I}}{d\tau} = \mu(\mathcal{V}_0 - \mathcal{V} - R\mathcal{I}). \tag{6}$$

Note that $\mathcal{F}(\mathcal{V})$ is an anti-symmetric function [i.e., $\mathcal{F}(-\mathcal{V}) = -\mathcal{F}(\mathcal{V})$], with a peak and a valley at $\mathcal{V} = -\mathcal{V}_m$ and $\mathcal{V} = +\mathcal{V}_m$, where $\mathcal{V}_m = \frac{1}{2}(V_v - V_p)$. Also, $\mathcal{F}'(\mathcal{V})$ is minimal at $\mathcal{V} = 0$, with $\mathcal{F}'(0) < 0$. The last step is to normalize the variables by defining, $v = \mathcal{V}/\mathcal{V}_m$, $y = \mathcal{I}/(\mathcal{V}_m|\mathcal{F}'(0)|)$, $r = |\mathcal{F}'(0)|R$, $m = \mu/|\mathcal{F}'(0)|$, $v_0 = \mathcal{V}_0/\mathcal{V}_m$, and $f(v) = \mathcal{F}(\mathcal{V})/(\mathcal{V}_m|\mathcal{F}'(0)|)$. Equations (5) and (6) now read as

$$m\frac{dv}{d\tau} = y - f(v), \tag{7}$$

$$\frac{dy}{d\tau} = m(v_0 - v - ry). \tag{8}$$

$f(v)$ is also anti-symmetric, with its peak and valley points at $v = -1$ and $v = +1$, respectively. Its derivative is minimal at the origin and unitary [i.e., $f'(0) = -1$]. Besides the assumptions made on the current–voltage characteristic $F(V)$, there is no loss of generality in the transformations leading from Eqs. (1) and (2) to Eqs. (7) and (8). All the variables and parameters, v, y, τ, r, v_0, and m, involved in Eqs. (7) and (8) are normalized in the sense that have no physical units. However, each one is linearly related to one original physical quantity, V, I, t, R, V_0, and μ, respectively. Therefore, we will refer to the normalized variables as voltage, current, time, resistance, input bias, and stiffness coefficient for the rest of this article. Likewise, we will refer to the normalized function $f(v)$ and its derivative as current–voltage characteristic and differential conductance.

B. Simplified current–voltage characteristic

A very simple choice for an origin-centered, anti-symmetric, N-shaped current–voltage characteristic with its peak and valley points at $v = \pm 1$ would be the third-degree polynomial,

$f(V) = \frac{1}{3}v^3 - v$. This choice turns Eqs. (7) and (8) into the FitzHugh–Nagumo (FHN) model.[18,19] The FHN model, however, does not reproduce bistability when the circuit's resistance is low. In contrast, bistability is observed in Ortega's work,[3] where Schulman's curve is used. Moreover, there is no other third-degree polynomial that satisfies the conditions mentioned above. This means that the shape of the polynomial curve cannot be tuned. Alternatively, a simple, tunable N-shaped curve can be made with a linear function minus a sigmoid. Such is the case in the Morris–Lecar model,[4,21] where the hyperbolic tangent is used. The Hodgkin–Huxley model[4,22] constitutes a more complex example, where the logistic function is used to model the ratio of open and closed voltage-gated channels in the neuron's cell membrane, such as the Na$^+$ and K$^+$ channels. The logistic function is also typically used in non-spike-based neural nodes.[23] In the simplified model proposed here, we choose the arctangent function since it leads to an approachable expression for the differential conductance, which in turn allows for a manageable derivation of the refractory time, in Sec. VI B,

$$f(v) = kv - h \arctan\left(\frac{v}{w}\right), \tag{9}$$

where $k, h, w > 0$. Consequently, the differential conductance reads as

$$f'(v) = k - \frac{hw}{v^2 + w^2}. \tag{10}$$

Provided that $h > kw$, then $f(v)$ is N-shaped, as it has a local maximum at $v = -v_M$ and a local minimum at $v = +v_M$, where $v_M = \sqrt{\left(\frac{h}{k} - w\right)w}$. These values delimit an NDC region embedded between two PDC regions. In particular, $f'(0) = k - \frac{h}{w} < 0$ is the minimal differential conductance. On the other hand, if $h \leq kw$, then $f(v)$ is monotonic and there is no NDC region.

The restrictions $v_M = 1$ and $f'(0) = -1$ constitute a system of two equations for k, h, and w, and its solution set can be computed as a parameteric form,

$$k = \frac{a}{1-a}, \quad h = \sqrt{\frac{a}{(1-a)^3}}, \quad w = \sqrt{\frac{a}{1-a}}, \tag{11}$$

where $0 < a < 1$. Note also that $kh/w = a$. Figure 2 shows some N-shaped curves given by Eqs. (9) and (11) for different values of a, which turns out to tune the sharpness of the curve. The smaller a, the spikier the peak and the valley of the current–voltage characteristic and the less curved the sections in the PDC and NDC regions. On the other hand, r and v_0 set the slope and position coefficient of the (normalized) load line, $v_0 - v - ry = 0$. Finally, it will be explained in Sec. III A that m levels the stiffness of the dynamics. Summarizing, Eqs. (7), (8), (9), and (11) define a simplified model with only four free parameters: a, r, m, and v_0. In what follows, the analytical expressions resulting from this simplified model will be computed in terms of k, h, w, or a, depending on what notation makes each expression more succinct. However, it is important to emphasize that k, h, and w are now defined as functions of a according to Eq. (11) and are not independent parameters.
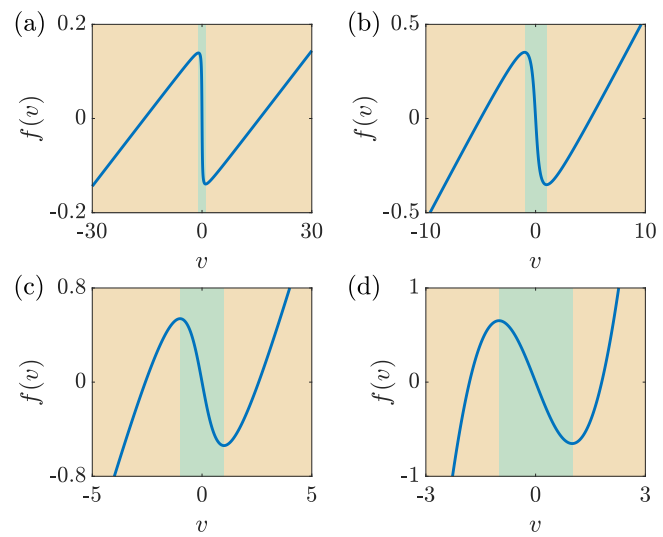
FIG. 2. Examples of normalized current–voltage characteristics used in the simplified model, Eqs. (7) and (8). The regions of positive and negative differential conductances are also shown as yellow and green areas, respectively. (a) $a = 0.01$, (b) $a = 0.1$, (c) $a = 0.4$, and (d) $a = 0.9$.

C. Equilibrium solutions

Depending on the parameters a, r, m, and v_0, the simplified model exhibits solutions in equilibrium in the form of fixed points [Fig. 3(a)] and limit cycles [Fig. 3(b)]. These solutions may be stable or unstable depending on the associated eigenvalues in the case of a fixed point and the Floquet multipliers in the case of the limit cycle.[24] There is also the possibility of multiple solutions coexisting. For instance, a stable fixed point and a stable limit cycle can coexist if an unstable limit cycle lies in between [Fig. 3(c)]. When this happens, we say that the system is *bistable*. It is also possible that the system exhibits multiple fixed points if the load line intersects the I–V curve in more than one place [Fig. 3(d)]. On this regard, the critical resistance, defined in Ref. 3 as the absolute value of the reciprocal of the minimal differential conductance in the NDC region, is significant. In the context of the simplified model, the critical resistance is a normalized quantity with no physical dimensions,

$$r_C = -\frac{1}{\min\{f'(v)\}}.$$

For the I–V characteristic defined in Eq. (9), the critical resistance is given by

$$r_C = -\frac{1}{f'(0)} = \frac{w}{h - kw},$$

which is reduced to 1 when k, h, and w are given by Eq. (11). Indeed, if the circuit's resistance is over the critical value, the load line may intersect the I–V curve in multiple points, with a maximum of three. Indeed, it is not difficult to demonstrate that looking for the intersection points is equivalent to intersecting a straight line with a sigmoid, which cannot intersect at more than three points.
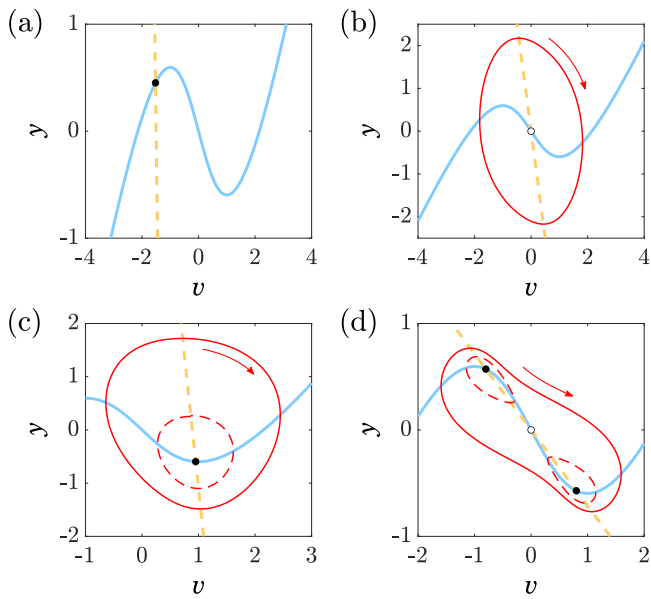
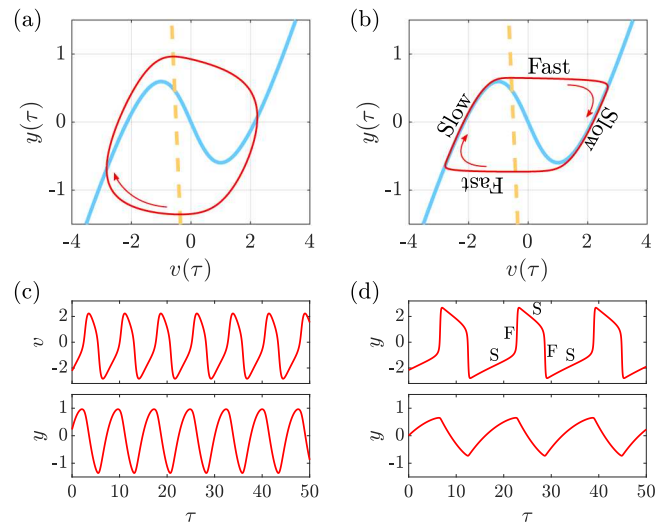**FIG. 3.** Stable and unstable solutions in equilibrium of Eqs. (7) and (8) under different parameters. Stable (unstable) fixed points are depicted as black (white) dots. Stable (unstable) periodic orbits are depicted as solid (dashed) red lines. The I–V characteristic (solid blue line) and load line (dashed yellow line) are included. (a) $a = 0.6$, $r = 0.05$. $m = 1.2$, $v_0 = -1.5$. (b) $a = 0.6$, $r = 0.2$, $m = 1.2$, $v_0 = 0$. (c) $a = 0.6, r = 0.1, m = 1, v_0 = 0.89$. (d) $a = 0.6, r = 1.4, m = 0.48$, $v_0 = 0$.

FIG. 4. Stable limit cycle on the phase space (solid red line) for $a = 0.6$, $r = 0.1$, $v_0 = -0.5$, and two different values of m: (a) $m = 0.4$ and (b) $m = 0.1$. The current–voltage characteristic (solid blue line) and load line (dashed yellow line) are included. (c) and (d) Evolution over time of the output variables v and y corresponding to the limit cycles in (a) and (b), respectively. The system exhibits stages of slow and fast dynamics when m is sufficiently small.

III. SPIKE GENERATION IN THE SIMPLIFIED MODEL

A. Slow–fast dynamics

It is often mentioned in the literature relevant to micro- and nanoscale RTDs that they exhibit self-sustained oscillations (i.e., a stable limit cycle) when biased in the NDC region and a steady response (i.e., stable fixed point) when biased in one of the PDC regions.[1,12,15] In general, the limit cycle is well-rounded and the dynamics is quite smooth [Figs. 4(a) and 4(c)]. However, if m is several times smaller than 1, the limit cycle in the simplified model takes a stiff shape and stages of slow and fast dynamics can be recognized [Figs. 4(b) and 4(d)]. In the stages of slow dynamics, the orbit remains close to the I–V curve in the PDC regions, until reaching either the peak or the valley, where the orbit quickly jumps toward the other PDC region. In this fast stage, the normalized voltage v suddenly changes in a very short time, with little change in the normalized current y. Thus, every period of the limit cycle has two slow stages and two fast stages. A physical interpretation of the slow–fast dynamics is provided by Ortega et al.[3] In the slow stages, $y \approx f(v)$, all the incident electrons cross the DBQW and none are accumulated in its ends (represented by the intrinsic capacitance C, see Fig. 1). In the upper fast stage, v suddenly raises and the DBQW charges. In the lower fast stage, v suddenly drops and the DBQW discharges.

How small the stiffness coefficient really needs to be for the system to exhibit slow–fast dynamics is actually subjected to the parameter a in the simplified model and to the specific shape of the

I–V curve in more realistic models and experiments. For $a = 0.6$, slow–fast dynamics is present for m under 0.1. However, if $a = 0.3$ (a rather sharp curve), m has to be reduced down to 0.05. In that sense, it is accurate to say that a also influences the stiffness of the dynamics.

B. Excitable response

Figure 4(d) shows that as a result of the slow–fast dynamics, an RTD biased in the NDC region produces spikes periodically (i.e., self-oscillations with a spike-like profile). It has been discussed in previous works[1,3,12] that an RTD can be configured to produce spikes in arbitrary fashion by setting the bias in the proximity to the NDC region and perturbing the circuit. If the perturbation is sufficiently strong, above a certain threshold, the system responds with a single spike (i.e., a single orbit, a precursor of the stable limit cycle) and returns to the stable fixed point equilibrium proper of a PDC-biased RTD. If the perturbation is weak, the system quickly returns to the fixed point and no spike is elicited. This property to respond only to suprathreshold perturbations is known as *excitability* and was first observed in neurological systems.[4,10,11] For the duration of the excitable response, known as refractory time, any additional perturbation—weak or strong—will not elicit a second response from the system.

Figure 5 shows that the simplified model, Eqs. (7) and (8), is able to reproduce the excitable behavior observed in RTDs. Here, the system is biased at the left side of the NDC region, close to the peak of the NDC region, and perturbed with a square voltage pulse, i.e., the input bias v_0 is changed for a brief time $\Delta\tau = 2$. For this configuration, in particular, the threshold value to trigger
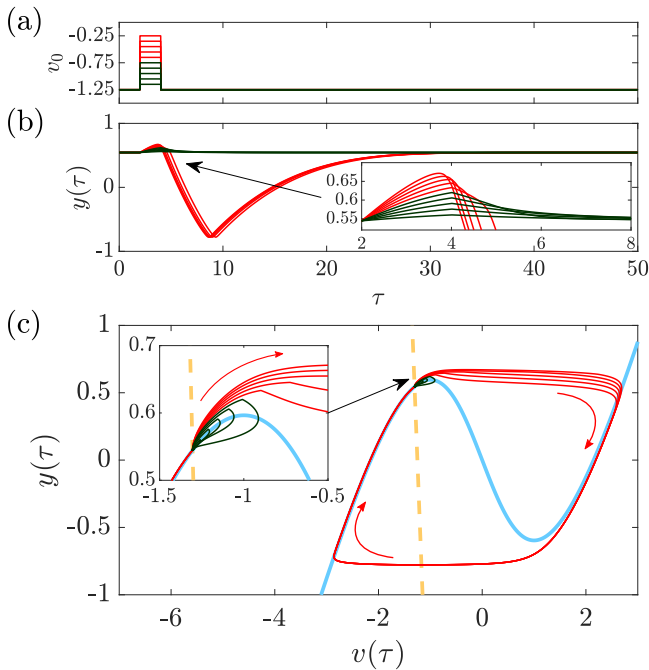
FIG. 5. (a) Square voltage pulses used to perturb the simplified model with parameters $a = 0.6$, $r = 0.1$, $m = 0.1$, and $v_0 = -1.25$. (b) Current responses to the perturbations over time. (c) Responses to the perturbations on the phase plane. Responses to suprathreshold perturbations exhibit stages of slow and fast dynamics. Suprathreshold (Subthreshold) perturbations and their responses are plotted in red (green). The insets zoom over the responses to sub-threshold perturbations.

the excitable response is $\Delta v_0 = 0.2$. If the amplitude of the square pulse is above Δv_0, a single down-stroke spike is elicited. Otherwise, the system quickly decays into the fixed point. It can be inferred from the anti-symmetry of the current–voltage characteristic curve that an excitable response in the form of an up-stroke spike can be achieved by biasing the RTD at the right side of the valley and injecting a negative square voltage pulse. More importantly, excitability in the simple model is a robust phenomenon in the sense that the model behaves as an excitable spike generator provided that it is biased close to the NDC region regardless of the other parameters or the shape of the I–V characteristic.

IV. BIFURCATION ANALYSIS

A. Bifurcation diagrams

The fixed point equilibrium solution to Eqs. (7) and (8) is given by the intersection between the RTD I–V characteristic $\left[y = f(v)\right]$ and the load line $\left(v_0 - v - ry = 0\right)$. This leads to the equation $v_0 - v - rf(v) = 0$, for which there is no analytical solution given our choice of the function $f(v)$. However, it is possible to derive a parametric form for the fixed point branch by computing the

coordinate v and the input bias v_0 as functions of the coordinate v,

$$v_0 = v + rf(v), \tag{12}$$

$$y = f(v). \tag{13}$$

Equations (12) and (13) can be used to trace a bifurcation diagram in terms of v_0 (see Fig. 6). Note that the shape of the branch is not affected by the stiffness coefficient m; its stability, however, is. The Jacobian matrix associated to Eqs. (7) and (8) reads

$$J = \begin{bmatrix} -\frac{1}{m}f'(v) & \frac{1}{m} \\ -m & -mr \end{bmatrix}.$$

The eigenvalues of J are given by

$$\lambda_\pm = \frac{1}{2}\left(\text{tr}(J) \pm \sqrt{\text{tr}(J)^2 - \det(J)}\right), \tag{14}$$

where the trace and determinant of J are in turn given by $\text{tr}(J) = -\left(\frac{1}{m}f'(v) + mr\right)$ and $\det(J) = rf'(v) + 1$. A fixed point (v, y) is stable if and only if both eigenvalues are either negative or complex conjugates with a negative real part. Andronov–Hopf (or simply, Hopf) bifurcations have been reported in previous studies on RTD models,[2,3] and they are also observed in this one (see Fig. 6). A Hopf bifurcation takes place when $\lambda_\pm$ are complex conjugates and their real part shifts sign,[4,24] i.e., $\text{tr}(J) = 0$ and $\det(J) > 0$. The first condition is satisfied when $v = \pm v_{AH}$, where v_{AH} is given by

$$v_{AH} = \sqrt{\frac{hw}{m^2 r + k} - w^2}. \tag{15}$$

It is inferred from Eq. (12) that two Hopf bifurcations occur at the input bias values $v_0 = \pm v_{AH} + rf(\pm v_{AH})$. This is possible only if v_{AH} is real, i.e., $m^2 r < \frac{h}{w} - k = 1$. Note that both $\pm v_{AH}$ are necessarily in the NDC region, since $f'(\pm v_{AH}) = -m^2 r < 0$. On the other hand, the second condition (evaluated at $v = \pm v_{AH}$) is satisfied when $mr < 1$.

Note that if $r \ll 1$, the $rf(v)$ term in Eq. (12) becomes negligible and the fixed point branch resembles the N-shaped I–V curve [see Fig. 6(a)]. As r increases, the branch adopts a more "italicized" shape [Fig. 6(b)]. However, if $r > 1$, the branch becomes a non-uniquely evaluated curve, as it folds back and forth into two saddle-node bifurcations [thus becoming Z-shaped, as seen in Fig. 6(c)]. It is geometrically intuitive that the saddle-node fixed point bifurcation occurs when dy/dv_0 diverges, i.e., $dv_0/dv = 1 + rf'(v) = 0$. The solutions to the latter equation are $v = \pm v_{SN}$, where v_{SN} is given by

$$v_{SN} = \sqrt{\frac{rhw}{1 + rk} - w^2}, \tag{16}$$

and we infer from Eq. (12) that the two saddle-node folds take place at $v_0 = \pm v_{SN} + rf(\pm v_{SN})$. The latter is possible only if v_{SN} is real, i.e., $r > \frac{w}{h - kw} = 1$. This is consistent with the results presented by Ortega et al.,[3] where saddle-node bifurcations arise only if the circuit's resistance is larger than the critical resistance.

The limit cycle branches shown in Fig. 6 have been numerically computed using MATLAB DDE-BifTool. From each Hopf bifurcation, a limit cycle branch emerges. The limit cycle may be stable
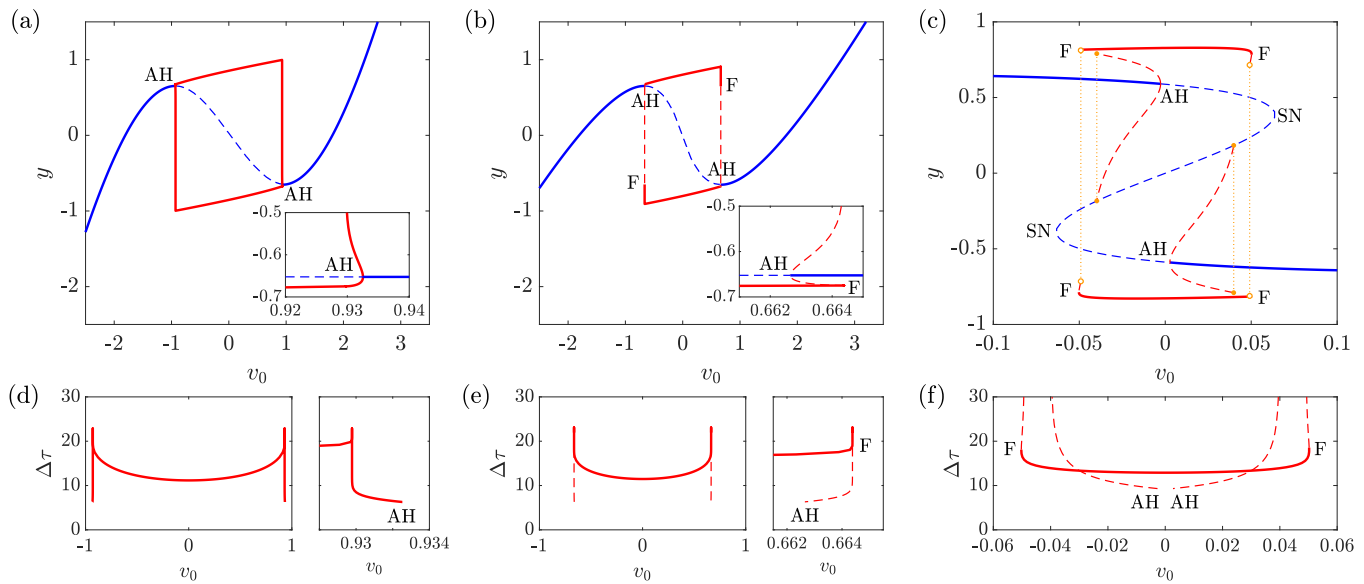
FIG. 6. Bifurcation diagrams over the input bias voltage v_0 for different values of a, r, and m. Solid (dashed) blue line: y-coordinate of the stable (unstable) fixed point. Solid (dashed) red line: y-extreme values of the stable (unstable) limit cycle. Solid (blank) yellow dots: y-extreme values of the small (big) homoclinic curves. AH, Andronov–Hopf bifurcations; SN, saddle-node bifurcations; F, limit cycle folds. Insets zoom over the right AH bifurcation. (a) $a = 0.9$, $r = 0.1$, $m = 0.2$; (b) $a = 0.9$, $r = 0.5$, $m = 0.2$; (c) $a = 0.9$, $r = 1.23$, $m = 0.6$. (d)–(f) Period of the limit cycles shown in (a)–(c). Right side boxes zoom over the right AH bifurcation.

or unstable depending on whether the Hopf bifurcation is super-critical or subcritical.[4,24] The nature of the Hopf bifurcation can be determined by a formula derived after a normal form analysis,[20,25,26]

$$\Omega = \frac{rf''(v_{AH})^2}{1 - (mr)^2} - f'''(v_{AH}). \qquad (17)$$

If Ω is negative (positive), the Hopf bifurcation is supercritical (subcritical) and the limit cycle is stable (unstable). The case of our interest is when RTD can behave as an excitable spike generator, i.e., m is very small. In that case, $\Omega \approx rf''(v_{AH})^2 - f'''(v_{AH})$. It turns out that $f'''(v_{AH}) = 2w(4kw - 3h) = \frac{8}{3}wh\left(a - \frac{3}{4}\right)$ [see Eq. (11)]. If $a > \frac{3}{4}$, then $f'''(v_{AH}) > 0$ and Ω may be positive or negative depending on r. For r sufficiently small, $\Omega < 0$, the Hopf bifurcations are supercritical and the limit cycle is always stable. Such is the case in Fig. 6(a). As r increases however, Ω becomes positive. The Hopf bifurcations are now subcritical and unstable limit cycle branches emerge from each one. These branches then fold (becoming stable) and connect, as shown in Fig. 6(b). As a consequence, there are ranges of v_0 where the system is bistable, as a stable fixed point and a stable limit cycle coexist [see Fig. 3(c)]. If m is small, these ranges are very narrow (order 10^{-3} or less) because the size of the limit cycle emerging from each Hopf point increases explosively with v_0 (thus being canard solutions[27]). On the other hand, if $a < \frac{3}{4}$, then $\Omega > 0$ and the system exhibits ranges of bistability regardless of r.

As a consequence of the fixed point branch becoming Z-shaped, the system may exhibit homoclinic bifurcations,[4] as illustrated in Fig. 6(c). The corresponding homoclinic solutions are shown in Fig. 7. As the limit cycle emerging from each Hopf point increases in size, it may encounter the middle fixed point, which

is a saddle with one attractive and one repulsive eigendirection. The limit cycle connects with these eigendirections and becomes a homoclinic curve that surrounds either the upper or the lower fixed point [Figs. 7(b) and 7(c), respectively]. This type of solution is known as "small" homoclinic curve.[4] Likewise, the unstable limit cycle coming from each fold may also coalesce with the middle saddle point and become a homoclinic curve. This coalescence is not visible in Fig. 6(c) because it occurs from the side of the saddle point rather than from above or below, but it can be appreciated in Figs. 7(a) and 7(d). These are known as "big" homoclinic curves because they surround the three fixed points.[4] Note that the homoclinic bifurcations result in discontinuities in the unstable limit cycle branches.

Figure 6(d)–6(f) show the period of the limit cycles depicted in Figs. 6(a)–6(c), respectively. As a limit cycle emerges from each Hopf bifurcation, its period increases explosively (regardless of whether the Hopf bifurcations are super or subcritical), reaches a peak value, and then decreases. Thus, the period exhibits a concave basin with a local minimum at $v_0 = 0$. It makes sense that the limit cycle period is a symmetrical curve of v_0 given the anti-symmetry of $f(v)$. The peak values of the limit cycle are not at the fold points (in case there is any) but slightly inward.

B. Bifurcation branches on the space of parameters

In this section, the evolution of the bifurcation branches is tracked in terms of the system parameters (a, m, r, v_0). In order to simplify this study, only the $m < 1$ case is considered, as our interest lays on the slow–fast dynamics and excitable response. In Sec. IV A, the input bias values for which the Hopf bifurcations and
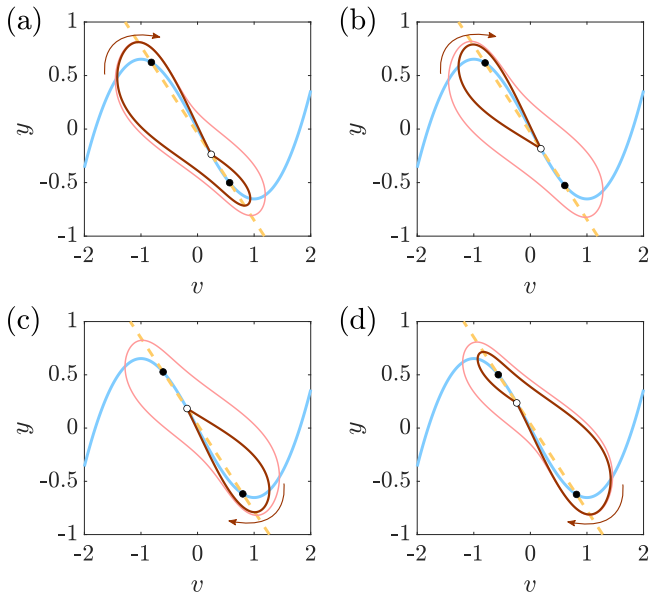
FIG. 7. Homoclinic solutions to Eqs. (7) and (8) (brown lines) for $a = 0.9$, $r = 1.23$, and $m = 0.6$ and different values of v_0. Stable (unstable) fixed points are depicted as black (white) dots. Stable periodic orbits and nullclines are included as light-shaded lines. (a) $v_0 = -0.049$ ("big" homoclinic); (b) $v_0 = -0.04$ ("small" homoclinic); (c) $v_0 = 0.04$ ("small" homoclinic); (d) $v_0 = 0.049$ ("big" homoclinic).

saddle-node bifurcations take place were computed,

$$v_0^{AH} = \pm \left(v_{AH} + rf(v_{AH}) \right), \quad (18)$$

$$v_0^{SN} = \pm \left(v_{SN} + rf(v_{SN}) \right), \quad (19)$$

where v_{AH} and v_{SN} are given by Eqs. (15) and (16), respectively. This allows to compute the Hopf and saddle-node branches in the plane of parameters defined by v_0 and r, as illustrated in Fig. 8. In panel (a), the remaining parameters are fixed at $a = 0.3$ and $m = 0.2$. Both bifurcations have actually two branches each with opposite v_0 values (the "±" acts as a common factor since in this simplified model, $f(v)$ is perfectly anti-symmetric). As r increases, the fixed point branch takes a more "italicized" N-shape and the Hopf points become closer. At $r = r_C = 1$, the fixed point branch becomes Z-shaped [see Fig. 6(c)] and the two saddle-nodes emerge from a cusp.[4] The saddle-nodes become more distant from one another with increasing r. Now that the fixed point branch is not uniquely evaluated, the Hopf points may switch sides. For $a = 0.3$ and $m = 0.2$, this occurs at about $r = 1.8$ [Fig. 8(a), lower-left panel]. As r further increases, the saddle-nodes approach the Hopf points and they coalesce at $r = \frac{1}{\mu} = 5$ in a Bogdanov–Takens bifurcation.[4] Here, the Hopf branches vanish, as discussed in Sec. IV A.

The Hopf branches delimit the regions where the fixed point is stable or unstable (see Fig. 8). As the fixed point-branch becomes Z-shaped and the Hopf points switch sides, a new region arises in the space of parameters where the system exhibits two stable fixed points in coexistence. This region is first delimited by the
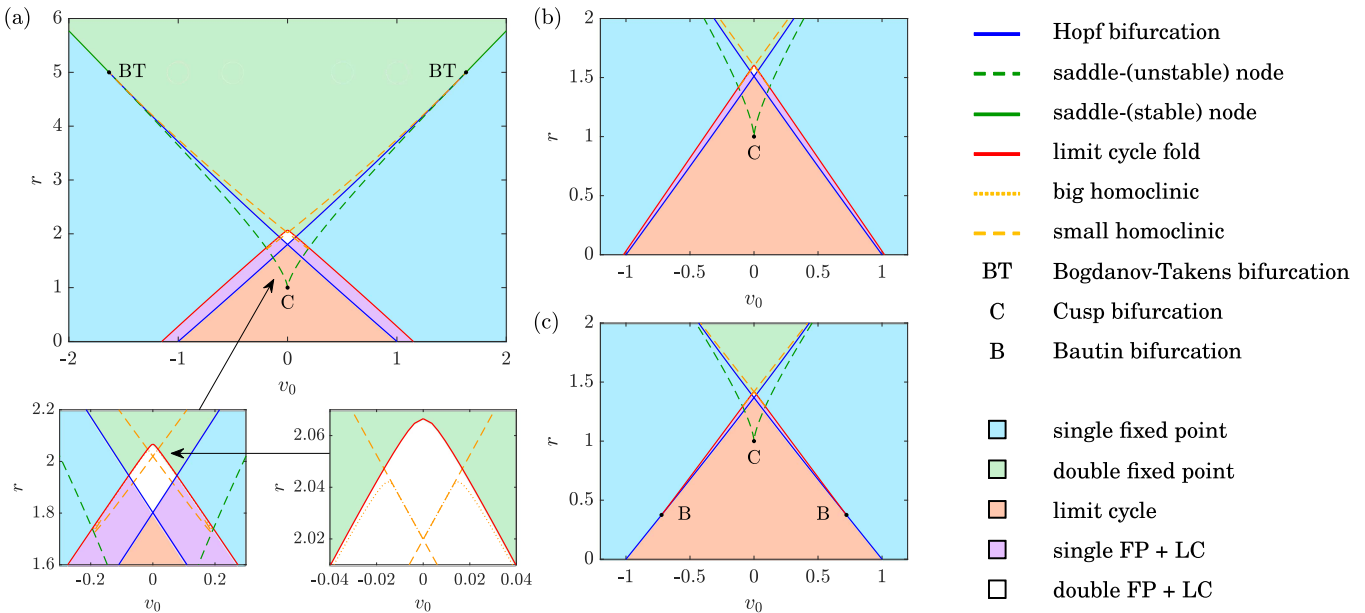
FIG. 8. (a) Bifurcation branches and stable solutions on the (v_0, r) plane for $a = 0.3$ and $m = 0.2$. The lower panels zoom over the triple stability region (double FP + LC). (b) and (c) Bifurcation branches and stable solutions on the (v_0, r) plane for (b) $a = 0.6$, $m = 0.3$ and (c) $a = 0.9$, $m = 0.4$.

Hopf branches. Above the Bogdanov–Takens bifurcations, there is no Hopf points and the region is delimited by the saddle-nodes. In order to understand this, it is worth computing the eigenvalues at the saddle-nodes. It was explained in Sec. IV A that at the saddle-nodes, $\det(J) = 1 + rf'(v) = 0$. Substitution in Eq. (14) leads to $\lambda_1 = 0$ and $\lambda_2 = \text{tr}(J) = -\frac{1}{m}f'(v) - mr = \frac{1}{mr} - mr$. The second eigenvalue is positive only if $r < \frac{1}{m}$. This means that for $r < \frac{1}{m}$, each saddle-node gives rise to an unstable node and a saddle (also unstable), with the former eventually transitioning into an unstable focus and then into a stable focus later at the respective Hopf point [see Fig. 6(c)]. On the other hand, for $r > \frac{1}{m}$, each saddle-node gives rise to a stable node and a saddle.

The limit cycle fold branches were numerically computed with MATLAB DDE-BifTool. When $a = 0.3$ and $m = 0.2$ [Fig. 8(a)], these branches remain close to each Hopf bifurcation at a distance mostly unchanged by r. As r increases, the folds become closer, and at about $r = 2.07$, they connect [Fig. 8(a), lower-right panel]. The limit cycle folds delimit the region where the system exhibits a stable limit cycle, and, together with the Hopf branches, they delimit the regions where the limit cycle coexists with a stable fixed point, i.e., the system is bistable. These two ranges of bistability intersect right under the peak of the limit cycle fold branches [Fig. 8(a), left panel]. In this intersection, the stable limit cycle coexists with two stable fixed points, i.e., the system exhibits a triple stability.

The homoclinic branches have also been computed with MATLAB DDE-BifTtool. These branches emerge close to the intersection between the saddle-node and Hopf branches at about $r = 1.74$ [Fig. 8(a), lower-left panel]; one small homoclinic and one big homoclinic from each side. If m is small, the homoclinic branches remain close to the limit cycle folds. As r increases, the homoclinics approach the v_0-axis. At about $r = 2.02$, the small homoclinics switch sides [Fig. 8(a), lower-right panel]. They do not coalesce, since each homoclinic surrounds a different fixed point. As r further increases, the small homoclinics approach the Hopf points, and they coalesce together with the saddle-nodes at the Bogdanov–Takens bifurcations at $r = \frac{1}{m}$ [Fig. 8(a), upper panel]. On the other hand, the big homoclinic branches fold at $r = 2.04$ and coalesce in the same point where the small homoclinics meet at $r = 2.02$. [Fig. 8(a), lower-right panel].

Figures 8(b) and 8(c) show the bifurcation branches and stable solutions on the (v_0, r) plane for $a = 0.6$ and $a = 0.9$, respectively. As the dynamics is more stiff, the branches are closer to one another and the regions of multiple stability are smaller. However, there is no changes on the qualitative basis, with the exception of the limit cycle fold at low resistance. If $a < \frac{3}{4}$ [Figs. 8(a) and 8(b)], the Hopf bifurcations are always subcritical; an unstable limit cycle branch emerges from each, which either folds to become stable or ends in a (small) homoclinic bifurcation. On the other hand, if $a > \frac{3}{4}$ and r is sufficiently small, the Hopf bifurcations are supercritical and a stable limit cycle branch emerges from each; there is neither limit cycle fold nor bistability. These arise when the Hopf bifurcations become subcritical (i.e., Bautin bifurcation[4]) when $\Omega = 0$ [see Eq. (17)]. The solution to this equation is numerically estimated at $r = 0.357 \pm 0.001$, in agreement with our results.

V. BISTABILITY RANGE

As explained in Sec. IV B, the limit cycle fold and the subcritical Hopf bifurcation at each side of the NDC region delimit a range on the v_0-axis where the stable limit cycle and the stable fixed point solutions coexist. This bistability is unwanted in the context of spike generation since it may lead to bursting.[4] From a didactic point of view, perturbing the circuit with a square voltage pulse equates to displacing the load line into the NDC region for a brief moment, which may trigger the stable limit cycle response. If the system has a sufficiently wide range of bistability, it will follow the cycle of hysteresis once the perturbation ends, which may have the system exhibit more than a single orbit of the limit cycle. The system may also exhibit stochastic bursting when injected with noise,[1–3] generating spikes at unwanted moments.

Figure 9 shows the bias range of bistability, Δv_0, for different values of a, r, and m. (Note that the ranges at both sides of the NDC region have the same size given the symmetry of the space of parameters, see Fig. 8.) We observe that for m under 0.1, Δv_0 increases with m at quadratic range, remaining under 0.01 in most cases [for comparison, remember that the peak and valley of $f(v)$ are at $v = \pm 1$]. It also increases with r and decreases with a although the influence of these parameters is little compared to that of m. As m increases above 0.1, Δv_0 increases at a less steep rate,
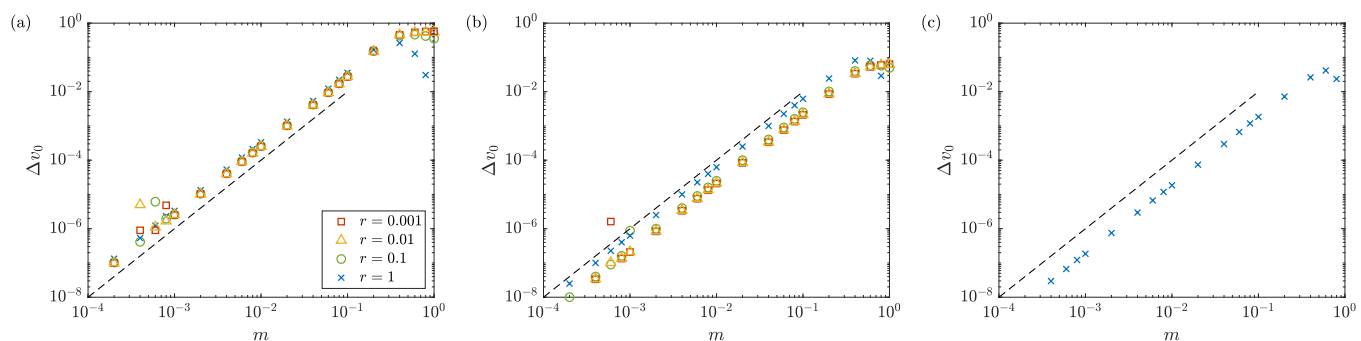
FIG. 9. Numerical estimation of the input bias bistability range as a function of m for different values of a and r. (a) $a = 0.3$; (b) $a = 0.6$; (c) $a = 0.9$. The dashed line marks the quadratic rate. Note that in (c) the system does not exhibit bistability only for $r \leq 0.1$. The outlayers in (a) and (b) are attributed to numerical imprecision.

reaches a maximum, and decreases. The size and position of maximum Δv_0 are both higher at higher r. Although not shown in the figure, Δv_0 is expected to become zero at a large, yet finite m, provided that $r \leq 1$. This has been observed by Ortega *et al.*[3] and it is also predicted by Eq. (17). From the discussion in Sec. IV A, we infer that the maximal value of m for which there is any Hopf bifurcation is $m = \frac{1}{\sqrt{r}}$. Since $\frac{1}{m}f'(v) + mr = 0$ at the Hopf point, we know that $f'(v_{AH}) = -m^2 r = -1$, the minimal negative differential conductance. Therefore, $f''(v_{AH}) = 0$ and $f'''(v_{AH}) > 0$. Thus, as m approaches $\frac{1}{\sqrt{r}}$, the first term in Ω approaches zero while the second term remains negative [see Eq. (17)]. Finally, Ω becomes negative, the Hopf bifurcations become supercritical and there is no bistability.

As discussed in Sec. IV A, if $a < \frac{3}{4}$ and m is small, the system exhibits bistability regardless of r. This is in agreement with Figs. 9(a) and 9(b). However, if $a > \frac{3}{4}$, the system exhibits bistability only for a sufficiently large resistance. Such is the case in Fig. 9(c), where $a = 0.9$, as there is a non-zero bias range only if $r = 1$. This is also in agreement with Eq. (17). Indeed, numerical computations show that for $a = 0.9$ and $r = 0.1, 0.01,$ and 0.001, the coefficient Ω is negative regardless of m.

It is worth comparing the results in this section with those presented by Carmona *et al.*,[?] where a 2D slow–fast model is studied. The nullclines are a piecewise linear N-shaped function and a vertical load line. This model can be interpreted as accounting for the dynamics of a zero-resistance RTD connected to DC voltage. In Carmona's work,[?] it is found that $\Delta v_0 = \alpha m + \beta m^{3/2} + O(m^2)$. This seems to contradict the quadratic rate relation reported here, although the N-shape curves used in both models are ultimately different in nature. Our choice of the N-shaped curve resembles a piecewise linear function for small values of a (under 0.1). It would be interesting to compute Δm_0 for small values of a, m, and r to establish a proper comparison between the models.

VI. LIMIT CYCLE PERIOD AND REFRACTORY TIME

A. Limit cycle period

A relatively simple expression for the period of the stable limit cycle can be provided when $m \ll 1$. To this end, an adiabatic approximation is applied, as illustrated in Fig. 10(a). During the first slow stage, the orbit remains over the I–V curve in the first PDC region. Upon arrival to the I–V curve peak at $v = -v_M = -1$, the orbit instantaneously and horizontally jumps to the second PDC region, at $v = v_A$, where $f(v_A) = f(-v_M) = y_A$. Here, the second slow stage takes place, and the orbit travels along the current–voltage characteristic until reaching the valley at $v = v_M = 1$. From here, there is another instantaneous, horizontal jump toward the first PDC region at $v = -v_A$, given by $f(-v_A) = f(v_M) = -y_A$. Although v_A cannot be computed analytically under our choice of $f(v)$, defined in Eq. (9), an approximation formula can be provided. In Fig. 10(b), numerical estimations of v_A for different values of a are plotted in a log–log scale and fitted against a quadratic polynomial via least squares regression; $\ln v_A = p(\ln a)$, where $p(x) = p_0 + p_1 x + p_2 x^2$ and $p_0 = 0.6862 \pm 0.0003$, $p_1 = -0.6487 \pm 0.005$, and $p_2 = -0.0133 \pm 0.0001$. Hence, v_A is approximated as

(a)

(b)

(c)
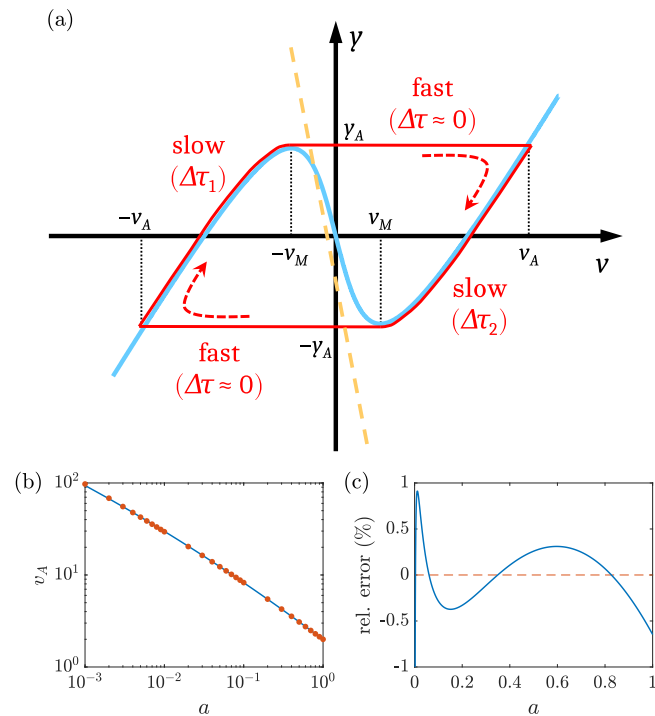
FIG. 10. (a) Schematics of the stable limit cycle under adiabatic approximation (solid red line). The nullclines are included as light-shaded lines. (b) Numerical computation of v_A as a function of a (orange dots), together with a quadratic fit of the logarithms (blue line). (c) Relative error of the quadratic fit as a function of a.

$e^{p(\ln a)}$. Figure 10(c) illustrates the relative error of the approximation, which remains under 1% for $a > 0.003$.

According to the adiabatic approximation, $y = f(v)$ during the slow stages, when the orbit travels over the I–V curve. Substitution of the latter in Eq. (8) allows to derive a one-dimensional equation for $v(\tau)$,

$$\frac{dv}{d\tau} = \frac{v_0 - v - rf(v)}{f'(v)}. \tag{20}$$

The period of the stable limit cycle is estimated as $\Delta\tau = \Delta\tau_1 + \Delta\tau_2$, where $\Delta\tau_1$ and $\Delta\tau_2$ are the duration of the first and the second slow stages, while the time spent at the fast stages is neglected. Integration of Eq. (20) over the intervals $[-v_A, -v_M]$ and $[v_A, v_M]$ leads to the following expressions for $\Delta\tau_1$ and $\Delta\tau_2$:

$$\Delta\tau_1 = \frac{1}{m} \int_{-v_A}^{-v_M} \frac{f'(v)}{v_0 - v - rf(v)}\, dv, \tag{21}$$

$$\Delta\tau_2 = \frac{1}{m} \int_{v_A}^{v_M} \frac{f'(v)}{v_0 - v - rf(v)}\, dv. \tag{22}$$

Thus, $\Delta\tau$ is inversely proportional to m. Numerical estimations of the limit cycle period reported by Ortega *et al.*[3] are in agreement with this. Remember that $\Delta\tau$ is the period in normalized units (see Sec. II B). Therefore, we expect the limit cycle

period in real time units to be directly proportional to the circuit's intrinsic inductance, L. This has been discussed by Romeira et al.[1] as well. For the piecewise linear model studied by Carmona et al.,[?] a more complex expression for the refractory time is derived. Moreover, the slow–fast parameter and variable normalization are different from those used here. Nonetheless, it can be demonstrated after proper variable conversion and Taylor expansion that $\Delta \tau \sim \left(1 + O(m^2)\right)/m$ when m is very small.

It is worth discussing the possibility of the integrand becoming singular [i.e., $rf(v) + v + v_0 = 0$] in Eqs. (21) and (22). This corresponds to the intersection of the nullclines at a fixed point. In principle, the stable limit cycle arises when the fixed point is unstable. This requires v to be in between $\pm v_{AH}$, which are in the NDC region, and in between $\pm v_M$ (see Sec. IV A). In this case, the singularity is in neither integration domain. It is also possible that the system is bistable and exhibits a stable limit cycle with a stable fixed point in one of the PDC regions, close to either $\pm v_M$. In this case, the integrand has a $\frac{1}{x}$-type of singularity and the corresponding integral is undefined. Nonetheless, the infinite areas under the curve at each side of the singularity have opposite signs and cancel out. (Likewise, the integral of $\frac{1}{x}$ between ± 1 is undefined, but the total area under the curve is zero.) In that sense, we say that the integral has a *principal value*.[28] The last scenario is that the fixed point is exactly at either $\pm v_M$. In this case, the integrand has a $\frac{0}{0}$ limit, found via L'Hôpital's rule to be $f''(\pm v_M)$, the singularity is repaired, and the integral converges.

Ortega et al. report that the refractory time is mostly unaffected by the circuit's resistance.[3] Together with the change of variables $v \to -v$ in Eq. (21) and the anti-symmetry of $f(v)$, this leads to

$$\Delta \tau = \frac{1}{m} \int_{v_M}^{v_A} \frac{2vf'(v)}{v^2 - v_0^2} \, dv. \tag{23}$$

Finally, substitution of $f'(v)$, V_M, and V_A allows to solve the above integral,

$$\Delta \tau = \begin{cases} \frac{1}{m}\left(\left(k - \frac{hw}{v_0^2 + w^2}\right) \ln\left|\frac{e^{2p(\ln a)} - v_0^2}{1 - v_0^2}\right| \\ + \frac{hw}{v_0^2 + w^2} \ln\left(\frac{e^{2p(\ln a)} + w^2}{1 + w^2}\right)\right), & |v_0| \neq 1, \\ \frac{k}{m} \ln\left(\frac{e^{2p(\ln a)} + w^2}{1 + w^2}\right), & |v_0| = 1. \end{cases} \tag{24}$$

Equation (24) is valid for v_0 between the Hopf bifurcation points ($\pm v_0^{AH}$) if they are supercritical and between the limit cycle fold points otherwise. Note that the upper expression in Eq. (24) is undefined when $v_0^2 = 1$, as the first logarithm has a diverging argument. However, the factor multiplying this logarithm turns out to be the differential conductance, $f'(v_0)$, which becomes zero when $v_0^2 = 1$. Thus, we have a $0 \times \ln(\infty)$ type of limit. It can be demonstrated that the limit when v_0^2 approaches 1 is, in fact, the lower expression in Eq. (24). This corresponds to the case discussed above, where the integrand singularity is at either -1 or $+1$ and can be repaired. Hence, the singularity in $\Delta \tau$ is also repaired.

In Fig. 11, numerical and analytical estimations of the stable limit cycle period are compared for different choices of parameters. Indeed, the analytical curve reproduces the concavity of the numerical curve along the v_0-axis and its valley at $v_0 = 0$. Both curves are in good agreement in most of the domains with a relative error of about
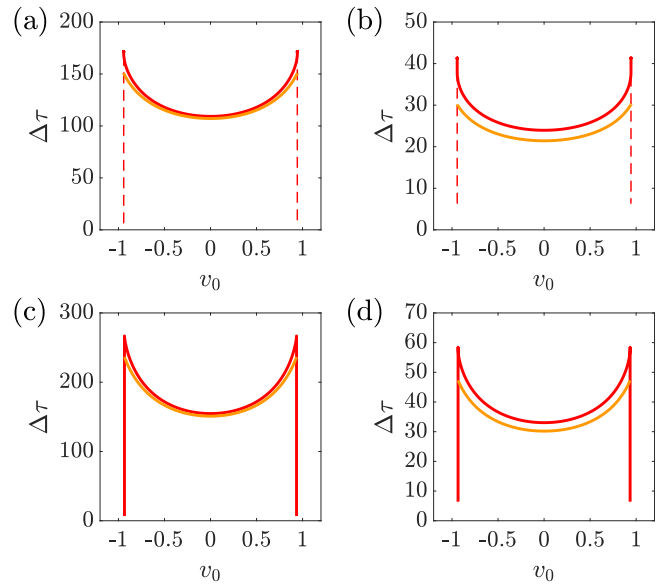

FIG. 11. Numerical estimation of the limit cycle period (red line) together with its analytical estimation (yellow line) as a function of v_0 for different values of a, r, and m. Stable (unstable) solutions correspond to solid (dashed) lines. (a) $a = 0.5, r = 0.1, m = 0.01$; (b) $a = 0.5, r = 0.1, m = 0.05$; (c) $a = 0.9, r = 0.1, m = 0.01$; (d) $a = 0.9, r = 0.1, m = 0.05$.

2% when $m = 0.01$ and 10% when $m = 0.05$. However, Eq. (24) loses validity at the boundaries of the domain, where the numerical curve reaches a peak and then decays, while the analytical curve continues to grow. This is even more notorious if the Hopf bifurcations are supercritical [Figs. 11(c) and 11(d)], since beyond the peaks the numerical estimation decays rapidly while the limit cycle remains stable. This loss of validity is expected at the boundaries, where the canard explosion takes place and the assumptions about slow–fast dynamics and adiabatic regime that led to Eqs. (21) and (22) are no longer valid.

B. Refractory time of the excitable response

The refractory time is the duration of the excitable response to a suprathreshold perturbation. During the refractory time, the system does not respond to any other perturbation, weak or strong. The excitable response is a single orbit, precursor of the stiff, stable limit cycle, with slow and fast stages, that takes place after a suprathreshold perturbation that momentarily drives the system into the region of the space of parameters where the stable periodic solution arises, beyond either a supercritical Hopf branch or a limit cycle fold branch. Therefore, the refractory time is expected to be similar to the limit cycle period close to the boundary of the aforementioned region. We propose Eq. (24) evaluated at $|v_0| = 1$ since it is a simple expression and close to the borders of the domain,

$$\Delta \tau_{\text{ref}} = \frac{k}{m} \ln\left(\frac{e^{2p(\ln a)} + w^2}{1 + w^2}\right). \tag{25}$$
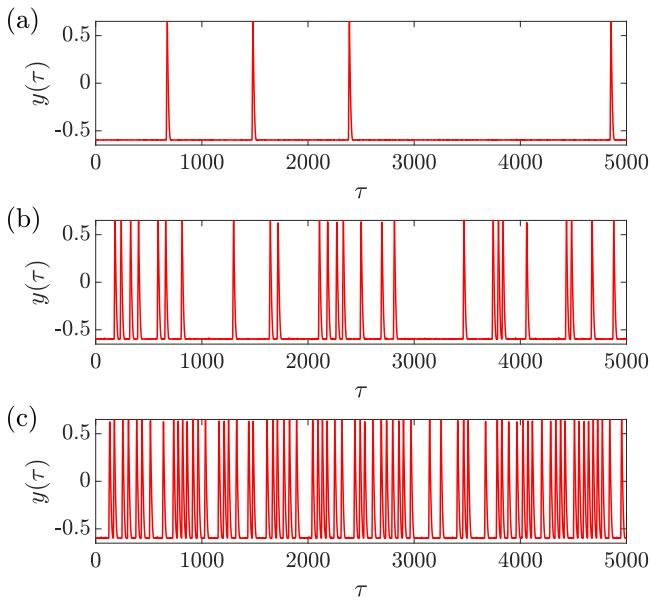
FIG. 12. Numerical simulations of Eqs. (26) and (27) for $a = 0.6$, $r = 0.1$, $m = 0.05$, $v_0 = 0.95$, and different values of η. (a) $\eta = 0.012$; (b) $\eta = 0.018$; (c) $\eta = 0.024$.

In order to check the validity of Eq. (25), numerical simulations of Eqs. (7) and (8) are carried out with additive noise,

$$\frac{dv}{d\tau} = \frac{y - f(v)}{m} + \eta\xi(\tau),$$ (26)

$$\frac{dy}{d\tau} = \mu(v_0 - v - ry).$$ (27)

Here, $\xi(\tau)$ is a time-uncorrelated white noise function [i.e., $\langle\xi(\tau)\rangle = 0$ and $\langle\xi(\tau_1)\xi(\tau_2)\rangle = \delta(\tau_2 - \tau_1)$) and η is the noise intensity. For given values of the parameters a, r, and m, the system is

biased at $v_0 = v_0^{\text{onset}} + \delta v_0$, where v_0^{onset} is the onset of the stable limit cycle at the right side of the current–voltage characteristic (either v_0^{AH} if the Hopf bifurcation is supercritical or the limit cycle fold point otherwise) and $\delta v_0 = 0.005$. Under this configuration, the deterministic system does not exhibit periodic solutions. However, provided that the fluctuations are sufficiently strong, excitable spikes are triggered randomly.[1–3] The higher the noise intensity, the more frequently spikes arise, as shown in Fig. 12. This can be used to estimate the refractory time as the shortest time in between two consecutive spikes over a simulation. The results are summarized in Fig. 13. Since the normalized refractory time $\Delta\tau_{\text{ref}}$ is inversely proportional to m, the actual refractory time in physical units is directly proportional to the circuit's inductance, L (see Sec. II). Figure 13 also shows that the refractory time decreases with increasing r and increases with increasing a. Still, m remains as the most influential parameter. This is consistent with the results reported by Ortega et al.[3] Figure 13 also shows good agreement between numerical and analytical estimations, with a relative difference under 2% provided that $r < 0.1$ and $\mu < 0.01$.

The possibility of chaos arising in the simplified model when biased close to a Hopf bifurcation or in between them and subjected to external modulation is an interest direction to conduct research on in a future study. Romeira et al.[2] investigate the effects of modulated dynamics on an RTD-based circuit, including mixed mode oscillations (MMOs) and potentially chaos as well as prospective applications in regenerative memory.

VII. SUMMARY AND CONCLUSIONS

A simple, bivariate mathematical model accounting for a DBQW-RTD connected to a DC voltage input has been proposed with the aim to find a proper configuration for the circuit to generate excitable spikes at arbitrary times. Instead of using Schulman's formula to represent the current–voltage characteristic of the RTD, as in previous works, a simple, N-shaped, origin-centered expression is chosen, consisting of a linear function minus an arctangent. Normalization of the variables and time leads to a further simplification of the model, now described in terms of four parameters: a, m, r, and v_0. These parameters tune the sharpness of the current–voltage
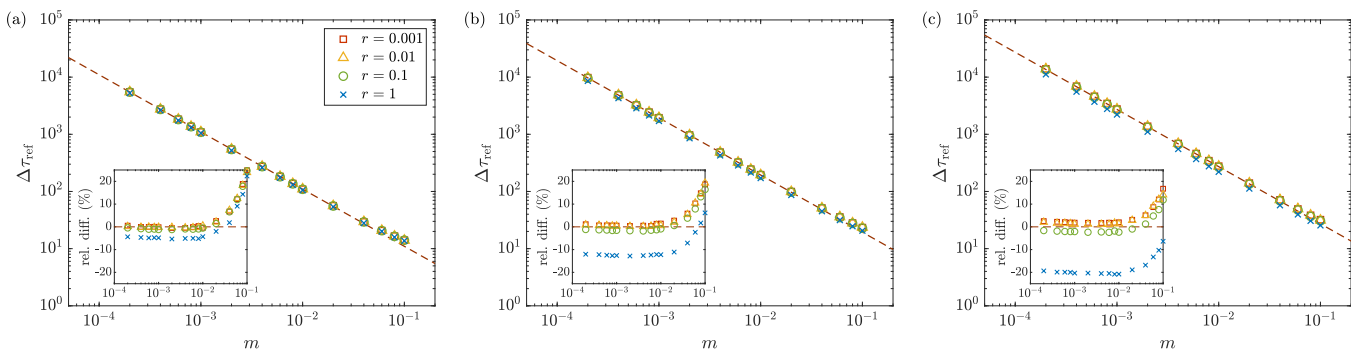
FIG. 13. Numerical estimation of the normalized refractory time of the excitable response as a function of m for different values of a, r, and η, together with its analytical estimation (dashed brown line). The insets show the relative difference between numerical and analytical estimations. (a) $a = 0.3$, $\eta = 0.05$; (b) $a = 0.6$, $\eta = 0.02$; (c) $a = 0.9$, $\eta = 0.02$.

characteristic, the stiffness of the dynamics (i.e., the rate between slow and fast time scales), the circuit's normalized resistance, and the input bias voltage, respectively. Depending on the parameters, the system exhibits solutions in equilibrium in the form of fixed point (i.e., steady response) or limit cycle (i.e., self-oscillations), with the possibility of coexistence between multiple solutions. The model is minimal in the sense that it is not possible to further reduce the number of parameters or variables without losing reproducibility of the observed phenomena described above.

The model successfully reproduces responses reported in previous theoretical works that use Schulman's curve.[1–3] A low resistance circuit exhibits self-oscillations when biased in the negative differential conductance region (delimited by the peak and valley of the I–V curve) and a steady response otherwise. As the resistance increases, the bias range where self-oscillations arise narrows and eventually vanishes. With the increase in the resistance, the system may also exhibit up to two stable fixed points coexisting (which may additionally coexist with the stable limit cycle), since the load line can intersect the current–voltage characteristic up to three times (the middle point always being a saddle). Provided that the stiffness coefficient m is sufficiently small, the self-oscillations show stages of slow and fast dynamics and thus spikes are generated periodically. If the circuit is biased outside but close to the bias range where self-oscillations arise and subjected to a suprathreshold perturbation (e.g., a square voltage pulse), it responds with a single orbit, precursor of the periodic spiking solution and therefore behaves as an excitable spike generator.

The bias voltage ranges where the circuit responds with a steady state or self-oscillations may overlap, thus producing ranges of bistability. From the nonlinear dynamics point of view, this occurs because the unstable limit cycle branch emerges from the fixed point at a subcritical Andronov–Hopf bifurcation, then folds and becomes stable. The criticality of the Hopf bifurcation is ruled by the sharpness of the I–V curve; if $a \leq 0.75$ (a relatively sharp I–V curve), there is always a bistability bias range. If $a > 0.75$ and the resistance is sufficiently small, the Hopf bifurcations are supercritical and there is no bistability. These results are in agreement with previous studies based on normal form expansion.[20,25,26] Bistability represents a drawback in the context of spike signaling since it may lead the circuit to respond to a single suprathreshold perturbation with multiple spikes (i.e., deterministic bursting). However, it is shown that for small-enough m, the bistability bias range is very narrow.

The choice of a simple N-shaped I–V curve allows to derive analytical expressions for the period of self-oscillations and the refractory time of the excitable response in the slow–fast regime. Both expressions are in good agreement with numerical simulations. In addition, both expressions, when normalized, are found to be inversely proportional to m. Consequently, the period and refractory time in actual time units are directly proportional to the circuit's inductance, L. This contradicts (or rather, amends) the notion suggested in prior studies[3] that the period and refractory time are similar to the tank period, $\sqrt{CL}$, where C is the RTD parasitic capacitance. The dilemma that these results present is that reducing L reduces the refractory time but may also compromise the slow–fast regime, since $m \propto \sqrt{C/L}$. To avoid this, C must be chosen to keep m small. Finally, the resistance has little effect on the refractory

time. Still, it is desirable to have a small resistance to avoid energy dissipation and coexistence of multiple fixed points.

The results presented in this work may serve as a guideline for prospective attempts to design and fabricate neuromorphic processors for time and power-efficient execution of machine learning algorithms and neural networks, where nanoscale RTD-based units would function as individual spiking signaling nodes. Under no circumstance, the simplified model intends to be a quantitatively accurate or a physically faithful representation of the dynamics of RTDs. The N-shaped current–voltage characteristic of an RTD is typically irregular and with no recognizable symmetry with respect to the NDC region. Furthermore, it tends to be even rougher for nanoscale RTDs, where the quantum effects become more pertinent, in contrast to the smooth and anti-symmetrical curve used in this study. All the latter must be considered in eventual attempts to model neural networks that resort to our simplified model to represent individual nodes, which may still have theoretical, computational, and applicational interests, especially considering the reduced number of parameters and lower power consumption.

In regard to biological neurons, the simplified model as presented here is in principle not suitable for reproducing their dynamics. Biological neurons are more complex systems than RTDs; a wider variety of phenomena and behaviors have been observed (such as class-1 excitability and spiking with long latency[4]) and their models generally involve more dynamic variables, equations, and parameters. The Hodgkin–Huxley model[4,22] and the Morris–Lecar model[4,21] are well-known examples, where the conductance of the neuron's cell membrane is accounted for by one or more time-dependent variables related to the voltage-gated channels that activate, deactivate, and/or inactivate depending on the membrane polarization voltage. In a more recent work by Yang *et al.*,[29] a multicompartment conductance-based neuron model is used to implement an architecture for neural networks. On the other antipode, minimal models have also been proposed to describe spiking in biological neurons, such as the integrate-and-fire models.[4,30] However, an approach similar to ours can also be applied to simplify biological neuron models and provide manageable and qualitatively reliable descriptions of the phenomena of interest. For instance, the Morris–Lecar model can be simplified in terms of the number of parameters and analytical complexity by using a linear-minus-sigmoid function with few parameters to reproduce the N-shaped nullcline and a single sigmoid to represent the S-shaped nullcline. Yang's architecture[29] might also see performance benefits by a similar simplifying approach. The chosen sigmoid may not necessarily be the hyperbolic tangent and its choice may be based purely on analytical manageability.

AUTHOR DECLARATIONS

Conflict of Interest

The authors have no conflicts to disclose.

DATA AVAILABILITY

The data that support the findings of this study are available from the corresponding author upon reasonable request.

REFERENCES

[1] B. Romeira, J. Javaloyes, C. N. Ironside, J. M. L. Figueiredo, S. Balle, and O. Piro, "Excitability and optical pulse generation in semiconductor lasers driven by resonant tunneling diode photo-detectors," Opt. Express **21**, 20931–20940 (2013).

[2] B. Romeira, J. M. L. Figueiredo, and J. Javaloyes, "Delay dynamics of neuromorphic optoelectronic nanoscale resonators: Perspectives and applications," Chaos **27**, 114323 (2017).

[3] I. Ortega-Piwonka, O. Piro, B. Romeira, and J. Javaloyes, "Bursting and excitability in neuromorphic resonant tunneling diodes," Phys. Rev. Appl. **15**, 034017 (2021).

[4] E. M. Izhikevich, *Dynamical Systems in Neuroscience: The Geometry of Excitability and Bursting, Computational Neuroscience* (MIT Press, Cambridge, MA, 2007).

[5] J. N. Schulman, H. J. De Los Santos, and D. H. Chow, "Physics-based RTD current-voltage equation," IEEE Electron Device Lett. **17**, 220–222 (1996).

[6] P. A. Merolla, J. V. Arthur, R. Alvarez-Icaza, A. S. Cassidy, J. Sawada, F. Akopyan, B. L. Jackson, N. Imam, C. Guo, Y. Nakamura, B. Brezzo, I. Vo, S. K. Esser, R. Appuswamy, B. Taba, A. Amir, M. D. Flickner, W. P. Risk, R. Manohar, and D. S. Modha, "A million spiking-neuron integrated circuit with a scalable communication network and interface," Science **345**, 668–673 (2014).

[7] "Intel Quark SE Microcontroller," Intel-SEEIM-4-2016.

[8] J. Robertson, M. Hejda, J. Bueno, and A. Hurtado, "Ultrafast optical integration and pattern classification for neuromorphic photonics based on spiking VCSEL neurons," Sci. Rep. **10**, 6098 (2020).

[9] J. Feldmann, N. Youngblood, C. D. Wright, H. Bhaskaran, and W. H. P. Pernice, "All-optical spiking neurosynaptic networks with self-learning capabilities," Nature **569**, 208–214 (2019).

[10] A. L. Hodgkin and A. F. Huxley, "A quantitative description of membrane current and its application to conduction and excitation in nerve," J. Physiol. **117**, 500–544 (1952).

[11] A. L. Hodgkin, A. F. Huxley, and B. Katz, "Measurement of current-voltage relations in the membrane of the giant axon of loligo," J. Physiol. **116**, 424 (1952).

[12] B. Romeira, J. Javaloyes, J. M. L. Figueiredo, C. N. Ironside, H. I. Cantu, and A. E. Kelly, "Delayed feedback dynamics of Liénard-type resonant tunneling-photo-detector optoelectronic oscillators," IEEE J. Quantum Electron. **49**, 31–42 (2013).

[13] R. Izumi, S. Suzuki, and M. Asada, "1.98 THz resonant-tunneling-diode oscillator with reduced conduction loss by thick antenna electrode," in *2017 42nd International Conference on Infrared, Millimeter, and Terahertz Waves (IRMMW-THz)* (IEEE, 2017), pp. 1–2.

[14] J. Wang, K. Alharbi, A. Ofiare, H. Zhou, A. Khalid, D. Cumming, and E. Wasige, "High performance resonant tunneling diode oscillators for THz applications," in *2015 IEEE Compound Semiconductor Integrated Circuit Symposium (CSICS)* (IEEE, 2015), pp. 1–4.

[15] J. Wang, A. Al-Khalidi, L. Wang, R. Morariu, A. Ofiare, and E. Wasige, "15-Gb/s 50-cm wireless link using a high-power compact iii-v 84-GHz transmitter," IEEE Trans. Microw. Theor. Tech. **66**, 4698–4705 (2018).

[16] S. Diebold, K. Nishio, Y. Nishida, J.. Kim, K. Tsuruda, T. Mukai, M. Fujita, and T. Nagatsuma, "High-speed error-free wireless data transmission using a terahertz resonant tunnelling diode transmitter and receiver," Electron. Lett. **52**, 1999–2001 (2016).

[17] B. Romeira, J. Figueiredo, and J. Javaloyes, "Nanoleds for energy-efficient and gigahertz-speed spike-based sub-λ neuromorphic nanophotonic computing," Nanophotonics **9**, 4149–4162 (2020).

[18] R. FitzHugh, "Mathematical models of threshold phenomena in the nerve membrane," Bull. Math. Biophys. **17**, 257–278 (1955).

[19] J. Nagumo, S. Arimoto, and S. Yoshizawa, "An active pulse transmission line simulating nerve axon," Proc. IRE **50**, 2061–2070 (1962).

[20] C. R. Wallis and S. W. Teitsworth, "Hopf bifurcations and hysteresis in resonant tunneling diode circuits," J. Appl. Phys. **76**, 4443–4445 (1994).

[21] C. Morris and H. Lecar, "Voltage oscillations in the barnacle giant muscle fiber," Biophys. J. **35**, 193–213 (1981).

[22] A. L. Hodgkin and A. F. Huxley, "A quantitative description of membrane current and its application to conduction and excitation in nerve," J. Physiol. **117**, 500–544 (1952).

[23] M. Nielsen, *Neural Networks and Deep Learning* (Determination Press, 2015), http://neuralnetworksanddeeplearning.com.

[24] S. H. Strogatz, *Nonlinear Dynamics and Chaos (With Applications to Physics, Biology, Chemistry and Engineering)* (CRC Press, 2015).

[25] A. A. Andronov, E. A. Leontovich, I. I. Gordon, and A. G. Maier, *Theory of Bifurcations of Dynamic Systems on a Plane* (Wiley, Jerusalem, 1973).

[26] J. Guckenheimer and P. J. Holmes, *Nonlinear Oscillations, Dynamical Systems, and Bifurcations of Vector Fields* (Springer, New York, 1983).

[27] E. Benoît, J. L. Callot, F. Diener, and M. Diener, "Chasse au canard (première partie)," Collectanea Mathematica **32**, 37–74 (1981).

[28] V. Carmona, S. Fernández-García, A. Teruel, "Saddle-node of limit cycles in planar piecewise linear systems and applications" Discrete Continuous Dyn. Syst. **39**, 5275–5299 (2019).

[29] R. P. Kanwal, *Linear Integral Equations: Theory and Technique* (Academic Press, New York, 2014).

[30] S. Yang, B. Deng, J. Wang, H. Li, M. Lu, Y. Che, X. Wei, and K. A. Loparo, "Scalable digital neuromorphic architecture for large-scale biophysically meaningful neural network with multi-compartment neurons," IEEE Trans. Neural Networks Learn. Syst. **31**, 148–162 (2020).

[31] L. Lapicque, "Recherches quantitatives sur l'excitation électrique des nerfs traitée comme une polarisation," J. Physiol. Pathol. Gen. **9**, 620–635 (1907).